


Article

Constructing Interconnected Hollow Mesopore Sn-Si Mixed Oxide Microspheres by Aerosol-Assisted Alkali Treatment with Enhanced Catalytic Performance in Baeyer-Villiger Oxidation

Qingrun Meng , Xiaoxu Gao, Dezheng Li and Huimin Liu *

Key Laboratory of Energy Chemical and Nano-Catalysis, School of Chemical and Environmental Engineering, Liaoning University of Technology, Jinzhou 121001, China; 18840177972@163.com (X.G.); ldz221882002@163.com (D.L.)

* Correspondence: meng081015@lnut.edu.cn (Q.M.); liuhuimin08@tsinghua.org.cn (H.L.)

Abstract: In this work, Sn-Si mixed oxide microspheres with concave hollow morphologies were first synthesized by a simple aerosol method using the very common commercial surfactant cetyl trimethyl ammonium bromide (CTAB) as a template, and then highly interconnected mesoporous and hollow Sn-Si mixed oxide microspheres were synthesized via an alkali (NaOH) treatment in the presence of CTAB. The results show that CTAB plays a crucial role not only in forming hollow morphologies during the aerosol process, but also protecting the amorphous framework and thus preventing the excessive loss of Sn species during the NaOH treatment. More importantly, it widens mesoporous distribution and forms interconnected mesoporous channels. The catalytic performance of Baeyer–Villiger oxidation on the interconnected mesoporous and hollow Sn-Si mixed oxide microspheres with 2-adamantanone and hydrogen peroxide was 9.4 times higher than that of the sample synthesized without the addition of CTAB; 2.3 times that of the untreated parent, which was due to the excellent diffusion properties derived from the hollow and interconnected mesopore structure. This method is mild, simple, low-cost, and can be continuously produced, which has the prospect of industrial application. Furthermore, the fundamentals of this study provide new insights for the rational design and preparation of highly interlinked mesoporous and hollow metal-oxides with unique catalytic performances.

Keywords: aerosol process; Sn-Si mixed oxide microspheres; interconnected hollow mesopore; alkali treatment; Baeyer–Villiger oxidation



Citation: Meng, Q.; Gao, X.; Li, D.; Liu, H. Constructing Interconnected Hollow Mesopore Sn-Si Mixed Oxide Microspheres by Aerosol-Assisted Alkali Treatment with Enhanced Catalytic Performance in Baeyer–Villiger Oxidation. *Catalysts* **2023**, *13*, 1494. <https://doi.org/10.3390/catal13121494>

Academic Editor: Lucjan Chmielarz

Received: 17 November 2023

Revised: 4 December 2023

Accepted: 4 December 2023

Published: 6 December 2023



Copyright: © 2023 by the authors. Licensee MDPI, Basel, Switzerland. This article is an open access article distributed under the terms and conditions of the Creative Commons Attribution (CC BY) license (<https://creativecommons.org/licenses/by/4.0/>).

1. Introduction

Baeyer–Villiger (B-V) oxidation for transforming ketones into corresponding esters or lactones is of great significance, both in theory and in practice in the organic chemistry and enzymatic fields (B-V monooxygenases enzymes) [1–3]. Up to now, organic peracids such as peroxyacetic acid still participate as oxidants, which results in environmental and safety problems [3–5]. Using H₂O₂ instead of organic peracids as an oxidant has advantages such as lower costs [6–8] and being environmental friendly [9–11] and therefore, is being paid more attention. However, due to the limited oxidation ability of H₂O₂ when compared with organic peracids, the key is the synthesis of efficient catalysts.

Frameworks incorporated with Sn(IV) active sites such as Sn-Beta zeolite exhibit higher activity and selectivity in the B-V oxidation of ketones with H₂O₂, which due to their Sn Lewis acid sites activating carbonyl groups and subsequently utilizing non-activated H₂O₂ [12]. However, the rigorous synthesis conditions of Sn-Beta zeolite such as long crystallization time, usage of toxic fluoride, and the diffusion limitations of microporous zeolite limited their practical applications. Later, various types of Sn-based heterogeneous catalysts, such as Sn-dendrimer/polystyrene [13,14], Sn-MCM-41 [15], Sn/cellulose [16], and Sn-containing clay minerals [17] have been developed in the past decade.

Highlighting the role of diffusion in catalysis, Sn containing interconnected mesoporous networks and hollow structure materials could be effective catalysts for the oxidation of bulky ketones because these materials have some remarkable advantages such as short charge transport pathways, greatly enhancing diffusion efficiencies and both outer and inner surfaces for reaction sites [18–22]. Many alternative methods have been proposed to realize the production of materials with a mesoporous or hollow structure: mechanical milling, precipitation, sol-gel, and hydrothermal methods [18,23,24]. However, significant difficulties associated with the above methods remain: (1) insufficient process control; (2) the complexity of the processes; (3) high-cost processing; (4) the yield of the products; and (5) scaling up the process.

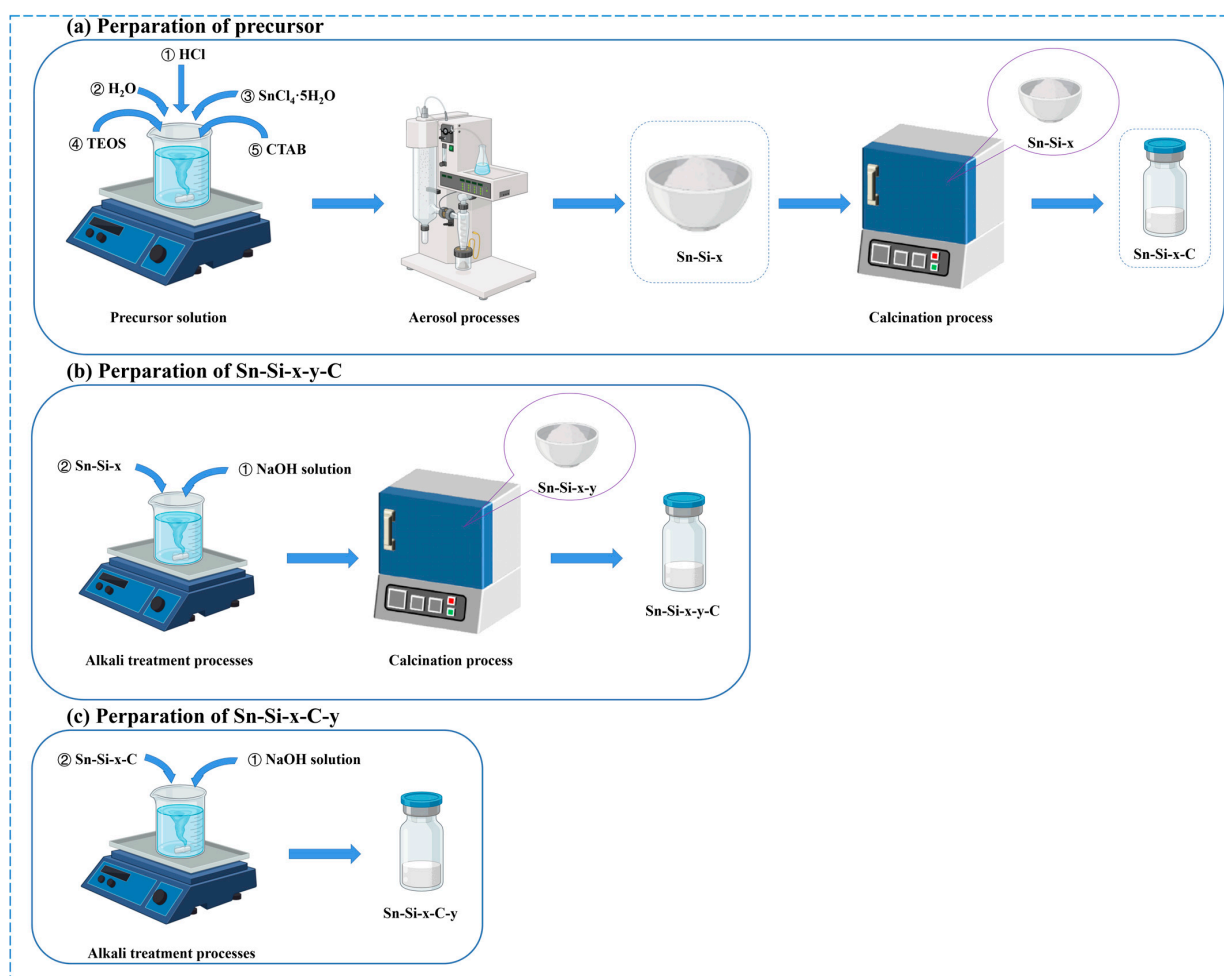
In recent years, an aerosol-assisted spray drying technique [25] has emerged as an innovative, versatile and effective way to produce various morphology and pore structure catalysts exhibiting new properties and high performances [26,27]. The method has significant advantages such as its rapid (only a few minutes) continuous mode and heteroatoms that are highly dispersed in the inorganic matrix [28–30]. Furthermore, the morphologies and pore structures of the products obtained by this method can be easily tuned just by modulating the composition of the precursor solution, which is very useful for designing high performance catalysts.

In this paper, highly interconnected mesopore and hollow Sn-Si mixed oxide microspheres have been successfully prepared via a simple and scalable aerosol-assisted alkali (NaOH) treatment using CTAB as the sole additive. In our synthesis strategy, OH^- ions, which induce desilication, are expected to occur only in the vicinity of the external surface due to the protection of CTAB. After the final calcination, Sn-Si mixed oxide microspheres with both abundant interconnected mesopores and hollow structures were obtained. The synthesis of Sn based materials with mesopores [29] or hollow structures [25] by the aerosol method has been reported, however, such materials with both abundant interconnected mesopores and hollow structures, especially using our simple, low-cost, and facile synthesis strategy have not been reported in the literature before. These unique features of Sn-Si mixed oxide microspheres can reduce diffusion limitations and improve access to active sites when used as catalysts. Therefore, the Baeyer–Villiger oxidation of the bulky substrate 2-adamantanone was selected as the model reaction to further demonstrate the advantages of such catalysts in terms of diffusion. It is proven that these catalysts exhibit high catalytic performance. This approach is generally applicable to other metal oxides (titanium-silica oxide, etc.) opening a new avenue to design and prepare such interconnected mesoporous and hollow structures with a high catalytic performance.

2. Results and Discussion

2.1. The Synthesis

The interconnected mesoporous and hollow Sn-Si mixed oxide microspheres were first synthesized by a simple aerosol method using CTAB as a template, and subsequently with an alkaline (NaOH) treatment (Scheme 1). The changes in morphology during the synthesis process can be observed by SEM, as shown in Figure 1. The morphology of the Sn-Si-C (without the addition of CTAB) sample exhibits a smooth solid sphere as shown in Figure 1a, which is consistent with our previous report [31]. Intriguingly, with the introduction of CTAB to the precursor solution, the as-synthesized Sn-Si-30 sample exhibits a concave hollow morphology as shown in Figure 1b. After calcination to remove CTAB, the Sn-Si-30-C sample presents a very similar concave hollow morphology as shown in Figure 1c. Therefore, it can be inferred that the formation of this concave hollow structure is attribute to the addition of CTAB that can cause a decrease in the surface tension of droplets during the aerosol process [32].



Scheme 1. Preparation of Sn-Si mixed oxide microspheres using different methods.

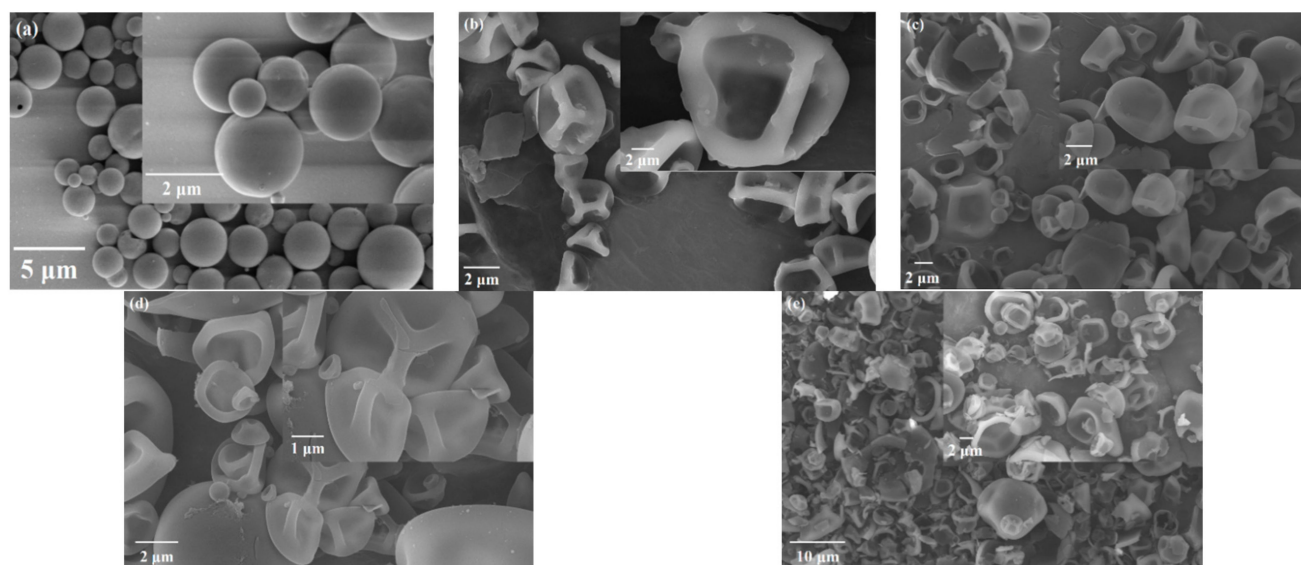


Figure 1. SEM images of (a) Sn-Si-C, (b) Sn-Si-30, (c) Sn-Si-30-C, (d) Sn-Si-30-0.1-C and (e) Sn-Si-30-C-0.1.

Sn-Si-30 and Sn-Si-30-C were subsequently treated with 0.1 M NaOH at room temperature for 1 h (Scheme 1b,c). The morphology of Sn-Si-30-0.1-C had no significant changes compared with Sn-Si-30, but the surface became relatively rough, as shown in Figure 1d.

Instead, the morphology of Sn-Si-30-C-0.1 generated more fragments (Figure 1e), which may have been due to the excess desilication by NaOH resulting in the collapse of the microsphere. These results indicated that CTAB, which existed in Sn-Si mixed oxide parent, inhibited excessive desilication by alkaline treatment and kept the amorphous framework and hollow morphology.

N₂ adsorption measurements were carried out to obtain the detailed porosity of the samples, as shown in Figure 2, the texture properties of which are summarized in Table 1. It was observed that the aerosol powder synthesized without the addition of CTAB (Sn-Si-C) was in a nonporous solid state, which was in agreement with SEM observations (Figure 1a). However, the Sn-Si-30-C sample showed the typical IV-type adsorption isotherm and H₂-type hysteresis loop in a relative pressure (p/p_0) range of 0.46–0.99 (Figure 2a), indicating the formation of the mesopores. The BJH pore size distribution evidences the formation of narrow mesopores centered at 2.1 nm (Figure 2b). The textural properties, such as BET specific surface area, mesoporous volume, and the proportion of the mesopores, were 1236 m²/g, 0.63 cm³/g and 84%, respectively, indicating that there were abundant mesopores in this sample (Table 1).

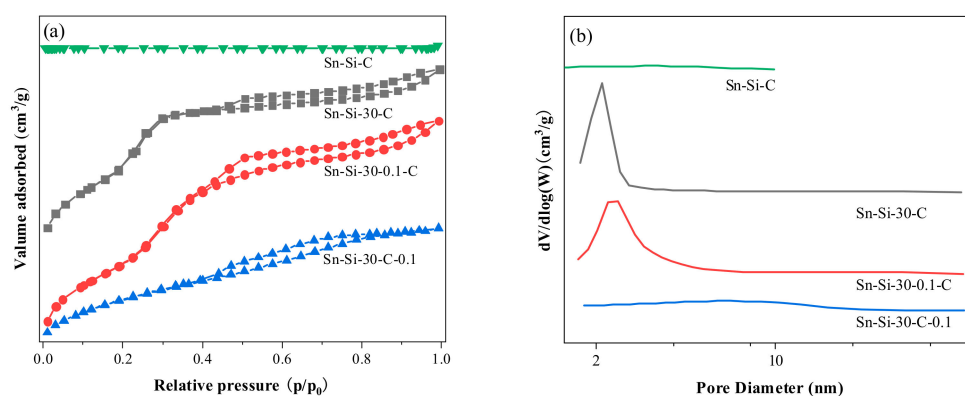


Figure 2. (a) N₂ adsorption–desorption isotherms and (b) BJH pore size distribution of the Sn-Si-C, Sn-Si-30-C, Sn-Si-30-0.1-C and Sn-Si-30-C-0.1.

Table 1. The textural properties of (1) Sn-Si-C, (2) Sn-Si-30-C, (3) Sn-Si-30-0.1-C and (4) Sn-Si-30-C-0.1 by N₂ physical adsorption.

Entry	Sample	Si/Sn ^a	S _{BET} (m ² /g) ^b	V _{total} (cm ³ /g) ^c	V _{meso} (cm ³ /g) ^d	V _{meso} /V _{total} (%)
1	Sn-Si-C	30	--	--	--	--
2	Sn-Si-30-C	29	1236	0.76	0.63	84
3	Sn-Si-30-0.1-C	51	1187	0.87	0.79	90
4	Sn-Si-30-C-0.1	83	549	0.47	0.38	80

^a Determined by ICP-OES; ^b BET surface area; ^c p/p_0 ; ^d mesoporous volume, $V_{\text{meso}} = V_{\text{total}} - V_{\text{micro}}$.

It is of interest that the treated Sn-Si-30-0.1-C sample showed a markedly bigger hysteresis loop in the relative pressure (p/p_0) range of 0.46–0.99, higher total volume (0.87 cm³/g), mesoporous volume (0.79 cm³/g), proportion of mesopores (90%), and extended BJH pore size distribution (Figure 2b) than that of the Sn-Si-30-C sample, implying an increase in the mesopore channels, which probably comes from the opening of the mesochannels. It should be noted that the BET specific surface area (1187 m²/g) of the Sn-Si-30-0.1-C sample is slightly lower than that of the Sn-Si-30-C sample, indicating that the mesoporous structures did not collapse during alkali treatment. On the contrary, the reference Sn-Si-30-C-0.1 sample shows dramatically decreased textural properties (Table 1), indicating the mesoporous structures were destroyed by alkali treatment. The above results evidently illustrate that the addition of CTAB to the precursor solution and after the aerosol process and calcination, a narrow mesopore centered at 2.1 nm can be formed.

Furthermore, during the alkali treatment, the presence of CTAB in the parent can further increase the amount of mesopores and extend the pore size distribution while protecting the mesoporous structure by suppressing excessive desilication. All of these results are consistent with those from the SEM measurements. To the best of our knowledge, this highly interconnected mesoporous and hollow Sn-Si mixed oxide with a big specific surface area has not been observed in the mesoporous materials reported in the literature before.

Sn-Si-30-C, Sn-Si-30-0.1-C, and Sn-Si-30-C-0.1 samples were also characterized by XRD patterns to check if there was a crystalline phase in the materials. All of these samples displayed a broad peak in the range of $2\theta = 20\text{--}30^\circ$ (Figure 3A), which can be assigned to the diffraction peaks of the amorphous silica from the walls [33]. The characteristic peaks of the SnO_2 crystalline phase could not be observed indicating that the Sn species were evenly dispersed on the silica matrix. The low-angle XRD patterns of these samples are also shown in Figure 3B. The Sn-Si-30-C sample displays (100) and (200) reflections of the ordered mesoporous lattice at 2.3 and 4.4° , respectively [34]. In the case of the treated Sn-Si-30-0.1-C sample (Scheme 1b), the intensity and position (2.3 and 4.4°) of the diffraction peak basically have no obvious changes, illustrating that the mesoporous regularity remained intact. However, a significant decrease in the intensity of the peaks corresponding to the reflections (100) or even their disappearance at (200) can be observed with the Sn-Si-30-C-0.1 sample (Scheme 1c), indicating the loss of mesoporous order, probably due to the excessive etching of NaOH. The above results fully demonstrate that the presence of CTAB in the parent can protect the mesoporous structure by suppressing excessive desilication during the alkali treatment and are consistent with the SEM (Figure 1) and N_2 adsorption–desorption (Figure 2) characterization.

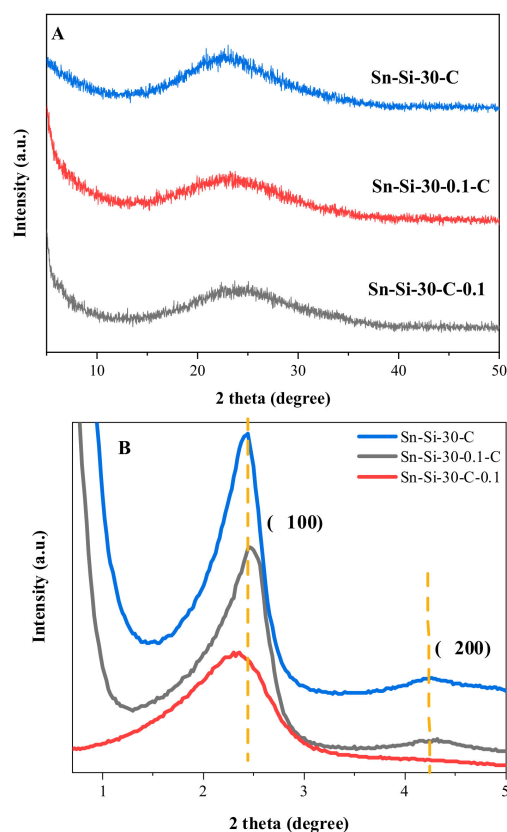


Figure 3. The high-angle (A) and low-angle (B) XRD patterns of Sn-Si-30-C, Sn-Si-30-0.1-C and Sn-Si-30-C-0.1 samples.

The FT-IR spectra of Sn-Si-30-C, Sn-Si-30-0.1-C, and Sn-Si-30-C-0.1 are shown in Figure 4. The samples exhibited peaks at the bands at 1080 , 800 and 460 cm^{-1} , which

is attributed to the asymmetric stretching vibration, symmetric stretching vibration, and bending vibration of Si-O-Si, respectively [35,36]. Clearly, the band at 960 cm^{-1} presents and is identified as the stretching vibrations of the Sn-O-Si linkages in the microspheres [37,38], indicating that the Sn atoms have been successfully incorporated in the SiO_2 framework.

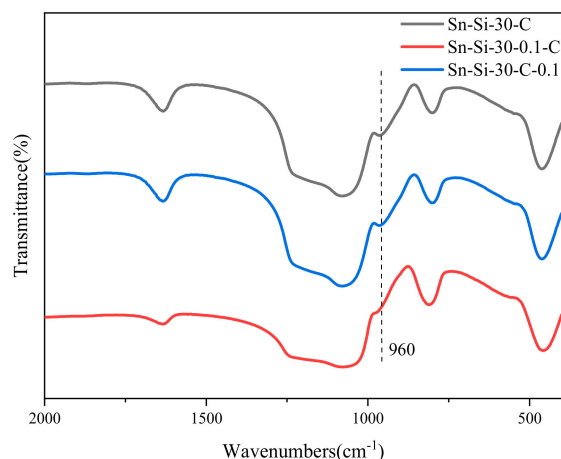


Figure 4. FI-IR spectra of the Sn-Si-30-C, Sn-Si-30-0.1-C and Sn-Si-30-C-0.1.

In order to further reveal the chemical nature and coordination states of the Sn species in the Sn-Si mixed oxide microspheres, the samples were characterized by UV-vis spectroscopy (Figure 5), which is normally adopted to determine the coordination environment of metal atom species in silica frameworks. The Sn-Si-30-C sample showed a main absorption band centered at 195 nm, which can be attributed to the presence of Sn(IV) in tetrahedral coordination within the silica framework [39–41]. The presence of small contributions at higher wavelengths (240 and 305 nm, respectively) can be assigned to extra-framework SnO_x clusters and bulk SnO_2 particles outside the framework [42,43]. It is known that the synthesis of Sn-Si mixed oxide proceeds via the hydrolysis of the precursors followed by condensation with the consequent formation of Sn-O-Si and Si-O-Si bonds, which are responsible for the formation of framework Sn(IV) species; however, due to the high Sn content in the precursor ($\text{Si}/\text{Sn} = 30$), a small amount of Sn species failed to incorporate into the framework and formed extra-framework Sn species during the spray drying or calcination processes. The actual Si/Sn molar ratios of the Sn-Si-C and Sn-Si-30-C samples (Table 1) are very close to those of the theoretical feed ratio, indicating that the loss of the Si and Sn source is avoided during the aerosol and calcination processes.

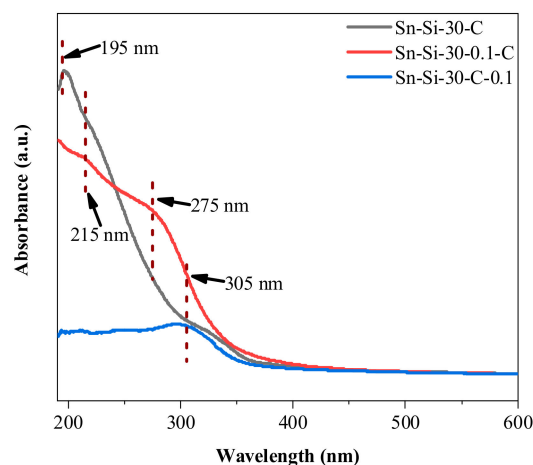


Figure 5. UV-Vis spectra of the Sn-Si-30-C, Sn-Si-30-0.1-C, and Sn-Si-30-C-0.1.

After the alkaline treatment, the Sn-Si-30-0.1-C sample showed two peaks centered at 215 nm and 275 nm, which are associated with the framework Sn(IV) species [44] and extra-framework SnO_x species, respectively [45]. The disappearance of bulk SnO_2 particles (305 nm), the decrease of the absorption peak of the framework Sn(IV) species, and a slight increase in the Si/Sn ratio indicate that a part of the Sn species dissolved from the microsphere, which most likely happened on its external surfaces. However, if the sample does not contain CTAB (Sn-Si-30-C-0.1), only an absorption peak at 305 nm which is assigned to bulk SnO_2 particles is observed, indicating that during the desilication process, most of the Sn(IV) species on the amorphous framework are shed and transform into SnO_2 particles. This agrees with the dramatic increase in the Si/Sn ratio of this sample. The above results indicate that the desilication process is accompanied by the loss of the amorphous framework Sn(IV). Meanwhile, the degree of desilication of Sn-Si-30-0.1-C is significantly lower than that of Sn-Si-30-C-0.1, indicating the protective effect of CTAB, which is consistent with the characterization of SEM and N_2 physical adsorption.

2.2. Mechanistic Investigation on the Role of CTAB

The above results fully illustrate that the introduction of CTAB played a crucial role in forming both the hollow and mesoporous structures, especially the protective effect during the desilication process. Therefore, the Sn-Si-30 parents were treated with various concentrations of NaOH to further explore the protective effect of CTAB. The morphologies of the treated samples were characterized by SEM (Figure S1). All alkali treatment microspheres showed a rough surface with various degrees of desilication. Compared to Sn-Si-30-0.05-C and Sn-Si-30-0.1-C, further increases in the concentration of NaOH lead to more deeply etched microsphere surfaces and collapsed frameworks.

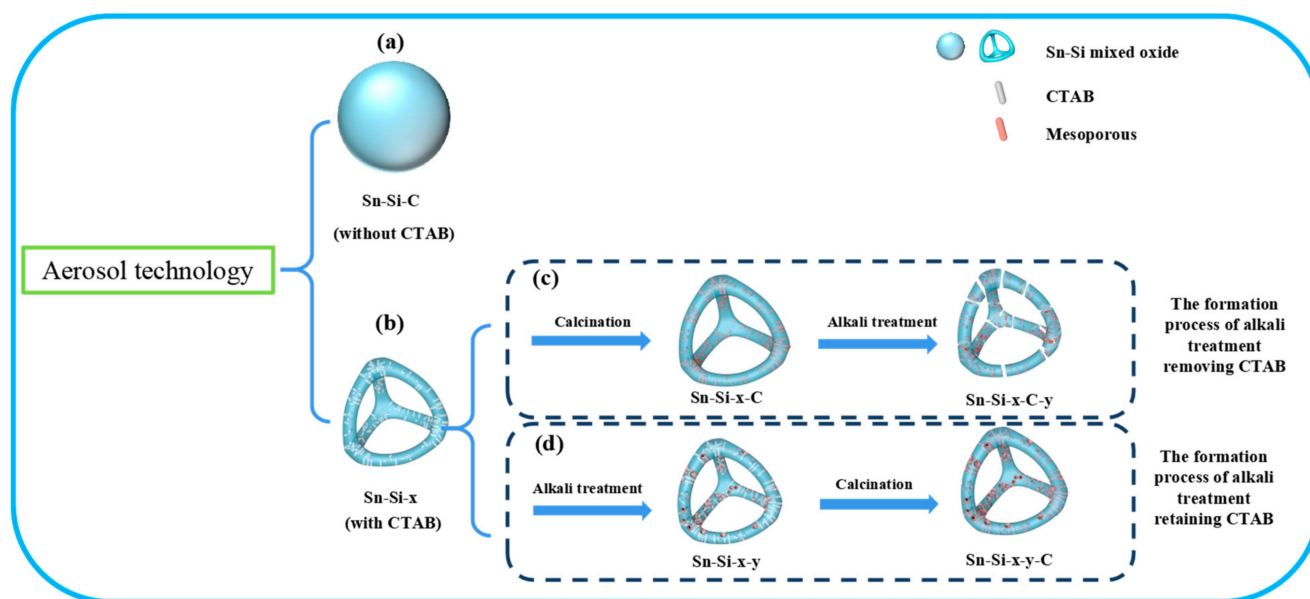
N_2 physisorption of the treated samples is shown in Figure S2. All samples (Sn-Si-30-y-C) show the typical IV-type adsorption isotherm and H_2 -type hysteresis loop in the relative pressure (p/p_0) range of 0.46–0.99, indicating the formation of the mesopores. The BJH pore size distribution in Figure S2b shows that Sn-Si-30-0.1-C has the widest mesoporous distribution. In addition, the texture properties of Sn-Si-30-y-C exhibit volcanic characteristics as shown in Table S1, the inflection point of which is Sn-Si-30-0.1-C. This sample presented the largest mesoporous volume ($0.79 \text{ cm}^3/\text{g}$), proportion of mesopores (90%), and specific surface area ($1187 \text{ m}^2/\text{g}$). The specific surface areas and pore structure parameters of the samples treated with high concentrations of NaOH (Sn-Si-30-0.3-C and Sn-Si-30-0.5-C) decreased indicating that this may be caused by SiO_2 framework dissolution, which is in line with the observations in SEM images.

The UV-Vis spectra of the Sn-Si-30-y-C (Figure S3) show that with increasing NaOH concentrations ranging from 0.05 M to 0.5 M, the absorption peak which is assigned to the framework Sn(IV) species (215 nm) gradually decreases until disappearing. Based on the above characterization results, the optimal concentration of NaOH treatment was 0.1 M.

Interestingly, using Sn-Si-30-C (without CTAB) as the parent, the obtained samples (Sn-Si-30-C-y) showed quite different results. Under the same alkali treatment conditions as described above, a drastic decrease in the specific surface areas (S_{BET}), mesopore volumes (V_{meso}), and total volumes (V_{total}) of the treated samples (Sn-Si-30-C-0.1 and Sn-Si-30-C-0.3) was observed when the NaOH concentration was higher than 0.1 M (Table S2), the corresponding BJH pore size distribution (Figure S5) shows the disappearance of the mesoporous distribution of these samples, suggesting that the amorphous framework collapsed and the mesoporous structure was destroyed by the etching of NaOH. In addition, the UV-Vis spectra reveal that the framework Sn(IV) species in the Sn-Si-30-C-y disappear as shown in Figure S5, indicating that the NaOH etching of the SiO_2 framework is accompanied by the loss of a large number of Sn(IV) species. These results indicate that the presence of CTAB in the parent during the NaOH treatment protects the amorphous framework from excessive etching and broadens the pore size distribution.

Inspired by the above discussion, a possible formation mechanism was proposed for the Sn-Si mixed oxide microspheres with different synthesis routes, as shown in Scheme 1.

The synthesis consists of two steps of aerosol and subsequent alkali treatments. If CTAB is not added in the precursor solution, a nonporous solid microsphere is obtained after the aerosol process (Sn-Si-C, Scheme 2a), which is consistent with our previous report [31]. Unexpectedly, a concave hollow morphology was observed after the same aerosol process when a certain amount of CTAB was introduced in the precursor solution (Sn-Si-x, Scheme 2b). This may be due to the decreased surface tension of the precursor solution derived from the addition of CTAB, which further leads to the droplets being distorted under the action of the purge gas. The solvent in the distorted droplet diffuses from the inside out and evaporates rapidly, and the solute assembles to form a rigid amorphous framework with a concave hollow morphology during the aerosol spray drying process. In this case, after calcination to remove CTAB, the Sn-Si mixed oxide microsphere (Sn-Si-x-C, Scheme 2c) also exhibited a concave hollow morphology but with an abundant mesoporous structure and very high specific surface area ($1236 \text{ m}^2/\text{g}$). However, in the subsequent alkali treatment, the amorphous framework of the microsphere severely collapsed, and the mesoporous structure was also destroyed (Sn-Si-x-C-y, Scheme 2c). This may be due to the presence of mesopores in the parent that allow OH^- to easily diffuse into the interior of the microsphere and thus the desilication process occurs on both the inner and the outer surfaces, resulting in the collapse of the framework structure by excessive etching and the abundance of mesopores as shown in Scheme 2c.



Scheme 2. The formation mechanism diagram of materials by aerosol technology and alkali treatment strategy.

On the contrary, using the CTAB-occluded microsphere as parent (Sn-Si-x), desilication induced by OH^- ions cannot penetrate the microsphere due to the presence of CTAB. Thus, desilication is expected to occur only in the vicinity of the external surface and mesopores are formed on the outer surface (Sn-Si-x-y, Scheme 2d). After calcination to remove CTAB, abundant mesopores are also formed in the interior of the microsphere. Compared with the untreated sample (Sn-Si-x-C), the obtained sample (Sn-Si-x-y-C) exhibited a slight decrease in the specific surface area ($1187 \text{ m}^2/\text{g}$), indicating that most of the amorphous framework and mesoporous structure were retained. More importantly, the increase in pore volume and the widening of the pore size distribution further indicate that the mesoporous structures on both the inner and the outer surfaces of the microsphere are interconnected (Scheme 2d).

2.3. Catalytic Performance Evaluation

In heterogeneous catalysis, not only the pore structure but also the number of active sites and the coordination state of the catalyst have a significant effect on the catalytic performance. It is known that the framework Sn (IV) species are the catalytic active center for B-V oxide reaction [29]. However, Sn-Si-30-0.1 also contains extra-framework SnO_x species (Figure 5), which may restrict its catalytic performance. Therefore, the range of the Si/Sn ratio needed to be further explored for the Sn-Si mixed oxide microspheres on the basis of the Sn-Si-x-0.1-C samples. It can be seen from the UV-Vis spectra shown in Figure 6 that all samples exhibit significant absorption peaks at 195–215 nm which are attributed to the tetrahedrally coordinated framework Sn species [39–41]. However, extra-framework Sn species also appeared in the samples with a higher Sn content (SnO_x clusters at 275 nm for Sn-Si-30-0.1-C and bulk SnO_2 particles at 305 nm for the Sn-Si-60-0.1-C). In addition, the absorption peak intensity of Sn-Si-90-0.1-C belonging to the framework Sn(IV) species (195 nm) was the highest, indicating the highest content.

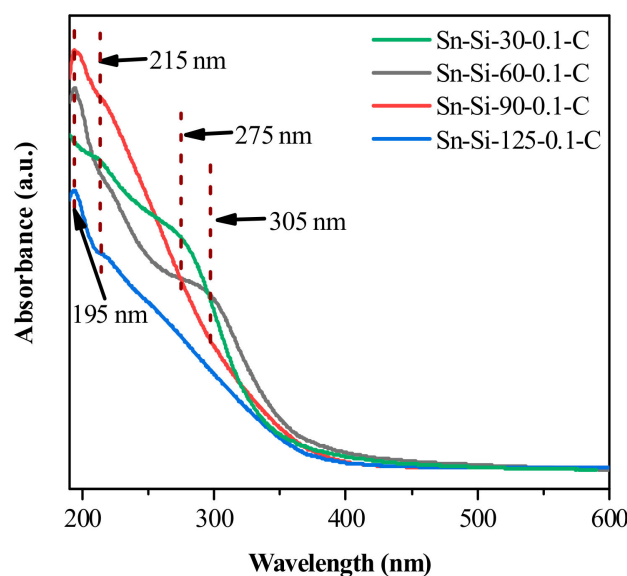
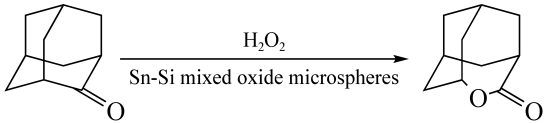


Figure 6. UV-Vis spectra of the Sn-Si-x-0.1-C.

In order to show the advantages of the diffusion performance in the Sn-Si mixed oxide microsphere, the Baeyer–Villiger oxidation of 2-adamantanone with H_2O_2 was performed over the prepared samples. As shown in Table 2, all of the samples show quite high selectivity to lactone, which should be due to its rigid structure. This is also in accordance with reports provided elsewhere [31]. The 2-adamantanone conversion of the Sn-Si-C is only 7%, which is due to its nonporous solid structure. With the addition of CTAB, Sn-Si-30-C presents a concave hollow morphology (Figure 1c), high surface area, and abundant mesopores (Table 1). The 2-adamantanone conversion of this sample thus increased by 29%. However, after the alkali treatment, the conversion of the Sn-Si-30-C-y samples (11–15%) was lower than the Sn-Si-30-C parent because of the collapsed amorphous framework (Figure S3) and severe loss of Sn active sites (Figure S4). On the contrary, the Sn-Si-30-y-C samples exhibit higher activity (26–50%). The concentration of the NaOH has an effect on catalytic performance. The highest conversion (50%) among these series of catalysts is obtained over Sn-Si-30-C-0.1, which should be well ascribed to the contribution of the interconnected mesochannels and extended pore size distribution. These results confirm the protective effect the CTAB on the framework and mesoporous structure during NaOH treatment, which prevents the excessive loss of Sn active sites. Surprisingly, the catalytic performance can be further improved by tuning the Sn/Si ratio in the Sn-Si-x-0.1-C sample. Sn-Si-90-0.1-C shows the best catalytic performance with 66% conversion, 2.3 times higher than that of the untreated sample (Sn-Si-30-C). These results demonstrate that the highly

interconnected mesoporous network and extended pore size distribution of Sn-Si mixed oxide play an overwhelming role in the tremendous increases of activity, while the number of Sn active sites also makes a considerable contribution.

Table 2. Comparison of Baeyer–Villiger oxidation of 2-adamantanone with H₂O₂ among varying Sn-Si mixed oxide microspheres ^a.



Entry	Catalyst	Conversion (%)	Selectivity (%)	Yield (%)
1	Sn-Si-C	7	99	7
2	Sn-Si-30-C	29	99	29
3	Sn-Si-30-C-0.05	11	99	11
4	Sn-Si-30-C-0.1	15	99	15
5	Sn-Si-30-C-0.3	13	99	13
6	Sn-Si-30-0.05-C	32	99	32
7	Sn-Si-30-0.1-C	50	99	50
8	Sn-Si-30-0.3-C	46	99	46
9	Sn-Si-30-0.5-C	26	99	26
10	Sn-Si-60-0.1-C	53	99	53
11	Sn-Si-90-0.1-C	66	99	66
12	Sn-Si-125-0.1-C	27	99	27

^a Reaction conditions: cat., 0.05 g; 2-adamantanone, 2 mmol; H₂O₂ (30%), 4 mmol; 1,4-dioxane, 10 mL; temp, 363 K; time, 180 min.

Another important factor for the evaluation of the catalyst is reusability. The Sn-Si-90-0.1-C catalyst was recovered by washing, drying, and calcination for the next run. Unfortunately, it can be seen from Figure 7 that a gradual decrease in 2-adamantanone conversion was observed during the five runs. A comparison of the texture properties derived from N₂ physical adsorption between the fresh and regenerated Sn-Si-90-0.1-C catalysts is shown in Table S3. A dramatic decrease in BET specific surface, total volume, and mesoporous volume was observed with the regenerated catalyst (Sn-Si-90-0.1-C-5), indicating the collapse of the mesoporous structure. In addition, the UV-Vis spectra of the regenerated catalyst revealed a loss of the framework Sn (IV) species and formed extra-framework SnO_x clusters (Figure 8). Therefore, the loss of activity (~28%) should be due to the collapse of the mesoporous structures resulting in the loss of Sn active sites (framework Sn (IV) species) and the change in the Sn coordinated environment (from framework Sn (IV) species to extra-framework SnO_x clusters). It should be noted that there is plenty of Si-OH available in the catalysts synthesized by the aerosol method [46]. The subsequent alkali treatment (desilication) process produces more Si-OH. Thus, it can be inferred that the Sn-Si mixed oxide microsphere catalyst synthesized in this manuscript should have a certain amount of Si-OH, which is easily attacked by water molecules resulting in the leaching of the framework Sn species. Thus, the reusability of Sn-Si mixed oxide microspheres in this study can be improved by increasing their hydrophobicity.

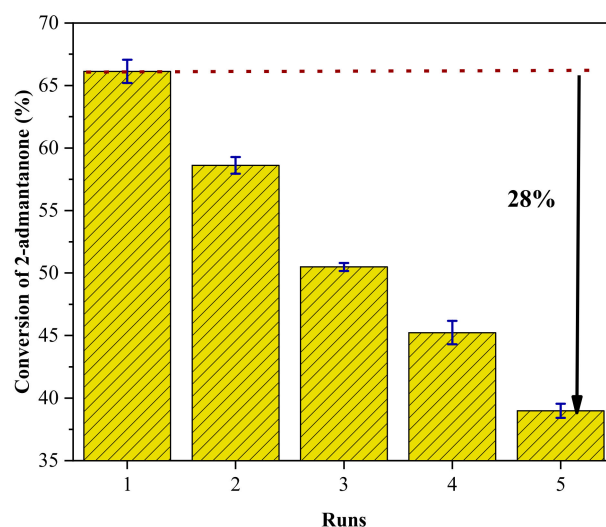


Figure 7. The reusability of the Sn-Si-90-0.1-C catalyst in the B-V oxidation of 2-adamantanone.

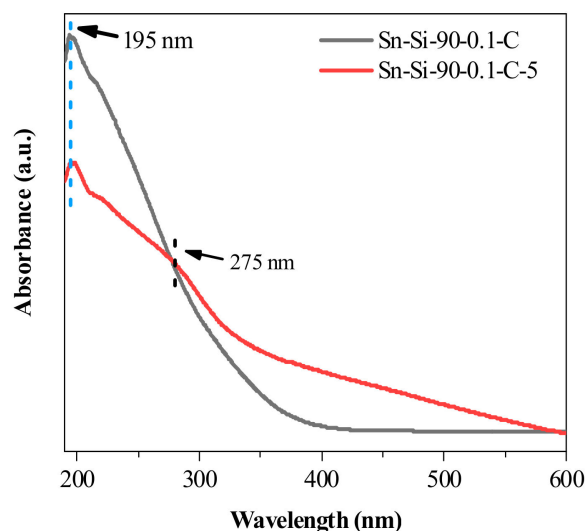


Figure 8. UV-Vis spectra of Sn-Si-90-0.1-C and Sn-Si-90-0.1-C-5.

3. Materials and Methods

3.1. Chemicals

The chemical reagents provided by Sinopharm Chemical Reagent Co., Ltd., Shanghai, China were as follows: tetraethyl orthosilicate (TEOS, analytically pure), stannic chloride pentahydrate ($\text{SnCl}_4 \cdot 5\text{H}_2\text{O}$, analytically pure), sodium hydroxide (NaOH, analytically pure), chlorobenzene ($\text{C}_6\text{H}_5\text{Cl}$, analytically pure), and 1,4-dioxane ($\text{C}_4\text{H}_8\text{O}_2$, analytically pure). Hexadecyl trimethyl ammonium bromide (CTAB, analytically pure) and 2-adamantanone (analytically pure) were from Macklin Biochemical Co., Ltd., Shanghai, China. Hydrochloric acid (HCl, 37%) was provided by Gucheng Chemical Reagent Co., Ltd., Jinzhou, China. Hydrogen peroxide (H_2O_2 , 30%) was provided by Damao Chemical Reagent Factory, Tianjin, China. Deionized water (DI) was self-made. The above chemical reagents were not purified further.

3.2. Synthetic Procedures

Preparation of the Sn-Si-x parent. The Sn-Si-x mixed oxide where “x” represented Si/Sn molar ratio in the initial solution was configured according to the molar composition ratio of 1.0 SiO_2 : (0.008–0.033) SnO_2 : 0.2 CTAB: 40 DI: 0.15 HCl. For a typical synthesis, solution A was prepared by dissolving a certain amount of tin (IV) chloride ($\text{SnCl}_4 \cdot 5\text{H}_2\text{O}$) in

a hydrochloric acid (HCl, 2.3 g) aqueous solution (55 g). Then, 32 g of tetraethyl orthosilicate (TEOS) was added. Cetyltrimethylammonium bromide (CTAB, 11 g) was dissolved in DI water (56 g) to yield solution B. Both solutions were left stirring for at least 2 h at room temperature. After that, solutions A and B were mixed together and then stirred for another 2 h to form a clear, transparent, uniform, and stable precursor solution. The precursor solution was converted into white SnO_2 - SiO_2 composite oxides by an aerosol spray dryer at 483 K and 800 mL/h. The obtained samples were dried at 373 K for 3 h as shown in Scheme 1a. For comparison, the Sn-Si-C (where “C” represented calcination) sample was also synthesized according to the above steps with $\text{SiO}_2/\text{SnO}_2 = 30$ and without adding CTAB. The sample was finally calcined under an air atmosphere at 823 K for 6 h.

Preparation of Sn-Si-x-y-C samples. The as synthesized Sn-Si-x parent was treated in a y M NaOH (y = 0.05, 0.1, 0.3 and 0.5) aqueous solution for 1 h at room temperature with the solid-liquid ratio of 1 g/10 mL, as shown in Scheme 1b. Subsequently, the treated samples were washed with DI for neutralization and dried overnight at 373 K. Finally, calcination (823 K for 6 h) was performed to remove the template (CTAB). The obtained samples were named Sn-Si-x-y-C (where “y” and “C” represented NaOH concentration and calcination, respectively).

Preparation of Sn-Si-x-C-y samples. As reference samples, the Sn-Si-x parent was first calcined under an air atmosphere at 823 K for 6 h to remove the template (CTAB) and then treated in an NaOH aqueous solution (y = 0.05 M, 0.1 M and 0.3 M). After washing with DI for neutralization and dried overnight at 373 K, the obtained samples were marked as Sn-Si-x-C-y, as shown in Scheme 1c.

3.3. Catalyst Characterization

Scanning electron microscopy (SEM, Carl Zeiss Jean company, Jena, Germany) operating at 200 kV was used to characterize the morphology of the mesoporous materials. The porous structures of all of the materials were measured by N_2 adsorption-desorption isotherm by an ASAP 2020 fully automatic physical adsorption analyzer of the American Micronics Company. The samples were treated at 573 K for 3 h prior to the analysis. Powder X-ray diffraction (XRD) patterns were recorded on a Shimadzu Rigaku D/Max 2400 diffractometer (Kyoto, Japan) with $\text{Cu-K}\alpha$ radiation at 40 kV and 10 mA. The low-angle diffraction diagrams of the samples were recorded in the 2 theta range of low-angles at 0.6 – 5° , with steps of 0.4° and a count time of 60 s at each point. The high-angle diffraction diagrams of the samples were recorded at a rate of $8^\circ/\text{min}$ in the range of 2 theta = 5 – 50° . FT-IR spectra were recorded in a range of 4000 – 400 cm^{-1} by a Bruker INVENIO S with spectral resolution of 4 cm^{-1} . The pore size distribution was calculated from the adsorption isotherm using the Barrett-Joyner-Halenda (BJH) method. The coordination status of Sn was detected by the UV-550 ultraviolet spectrophotometer of Jasco Company and barium sulphate powder was used as the reference sample. The Sn loadings were determined by inductively coupled plasma (ICP) analysis on a Perkin Elmer Optima2000DV inductively coupled plasma atomic emission spectroscope.

3.4. Performance Evaluation

Catalytic test. The catalytic evaluation of Baeyer-Villiger oxidation of 2-adamantanone and H_2O_2 was performed in a 25 mL round-bottomed flask. 2 mmol of 2-adamantanone, 10 mL of 1,4-dioxane, 0.05 g of the catalyst, 0.5 g of chlorobenzene (GC internal standard) [18,31], and 4 mmol of H_2O_2 (30%) were sequentially loaded into the reactor. The reaction was conducted at 363 K for 3 h. After cooling, the catalyst was removed by centrifugation and the reaction mixture was analyzed using a gas chromatograph (GC-7890, Techcom, Shanghai, China) equipped with a 30 m SE-54 capillary column and an FID detector (Techcom, Shanghai, China). The products were identified by using a GC-MS (Agilent-5975C).

Cycle test. The used catalyst was collected from centrifugation and washed with ethanol and DI, respectively. Subsequently, it was dried overnight at 373 K and calcined in a muffle furnace at a temperature of 823 K for 6 h for subsequent use.

4. Conclusions

In summary, highly interconnected mesoporous Sn-Si mixed oxide microspheres with a concave hollow morphology and large specific surface area ($\sim 1187 \text{ m}^2/\text{g}$) and mesoporous volume ($\sim 0.79 \text{ cm}^3/\text{g}$) have been successfully prepared exploiting a simple aerosol combined surfactant (CTAB) approach of first synthesizing hollow Sn-Si mixed oxide microspheres and subsequently with a NaOH treatment in the presence of CTAB. The characterization results show that CTAB has several key roles, such as the formation of a hollow morphology during the aerosol process, protection of the amorphous framework, prevention of the excessive loss of Sn species, the widening of the mesoporous distribution, and the formation of interconnected mesoporous channels during the NaOH treatment. Thanks to the unique interconnected mesoporous and hollow structure which can provide more accessible active sites opened by such an aerosol assisted alkali treatment approach, the optimized catalyst (Sn-Si-90-0.1-C) exhibits remarkably enhanced activity for the B-V oxidation of 2-adamantanone compared with the counterparts. This method is mild, simple, low-cost, and can be applied to improve the catalytic performances of the most industrially relevant metal oxides.

Supplementary Materials: The following supporting information can be downloaded at: <https://www.mdpi.com/article/10.3390/catal13121494/s1>, Figure S1: SEM image of Sn-Si-30-y-C series samples: (a,b) Sn-Si-30-0.05-C, (c,d) Sn-Si-30-0.1-C, (e,f) Sn-Si-30-0.3-C, (g,h) Sn-Si-30-0.5-C; Figure S2: (a) N_2 adsorption-desorption isotherms and (b) BJH pore size distribution of the Sn-Si-30-y-C series samples; Figure S3: UV-Vis spectra of the Sn-Si-30-y-C series samples; Figure S4: (a) N_2 adsorption-desorption isotherms and (b) BJH pore size distribution of the Sn-Si-30-y-C series samples; Figure S5: UV-Vis spectra of the Sn-Si-30-y-C series samples; Table S1. The textural properties of the Sn-Si-30-y-C series samples; Table S2. The textural properties of the Sn-Si-30-C-y series materials; Table S3. The textural properties of the Sn-Si-90-0.1-C and Sn-Si-90-0.1-C-5.

Author Contributions: Q.M.: conceptualization, supervision, writing—review and funding. X.G.: investigation, data curation, writing—original draft and editing. D.L.: Software. H.L.: conceptualization, supervision. All authors have read and agreed to the published version of the manuscript.

Funding: This work has been supported by Scientific Research Foundation of Liaoning province of China (JQL202015403), Natural Science Foundation of Liaoning Province (2020-BS-242).

Data Availability Statement: The data presented in this study are available on request from the corresponding author.

Conflicts of Interest: The authors declare that they have no known competing financial interest or personal relationship that could have appeared to influence the work reported in this paper.

Abbreviations

Sn-Si-x: Sn-Si mixed oxide synthesized by the aerosol process where “x” represents the Si/Sn molar ratio in the initial solution; Sn-Si-x-y-C: Sn-Si-x sample treated in an NaOH aqueous solution and calcination where “y” represents the concentration of NaOH and “C” represents calcination; Sn-Si-x-C-y: Sn-Si-x was first calcined and then treated in an NaOH aqueous solution where “C” represents calcination and “y” represents the concentration of NaOH; Sn-Si-C: Sn-Si mixed oxide synthesized by the aerosol process without the addition of CTAB followed by calcination where “C” represents calcination; Sn-Si-90-0.1-C-5: Sn-Si-90-0.1-C catalyst after five cycles; B-V: Baeyer–Villiger oxidation reaction.

References

1. Seo, E.-J.; Kim, M.-J.; Park, S.-Y.; Park, S.; Oh, D.-K.; Bornscheuer, U.; Park, J.-B. Enzyme access tunnel engineering in Baeyer–Villiger monooxygenases to improve oxidative stability and biocatalyst performance. *Adv. Synth. Catal.* **2022**, *364*, 555–564. [\[CrossRef\]](#)
2. Xu, H.; Jiang, J.; Yang, B.; Wu, H.; Wu, P. Effective Baeyer–Villiger oxidation of ketones over germanosilicates. *Catal. Commun.* **2014**, *55*, 83–86. [\[CrossRef\]](#)
3. Strukul, G. How green was my ester. *Nature* **2001**, *412*, 388–389. [\[CrossRef\]](#)
4. Sicard, R.; Chen, L.S.; Marsaioli, A.J.; Reymond, J.-L. A Fluorescence-Based Assay for Baeyer–Villiger Monooxygenases, Hydroxylases and Lactonases. *Adv. Synth. Catal.* **2005**, *347*, 1041–1050. [\[CrossRef\]](#)
5. Michelin, R.A.; Sgarbossa, P.; Scarso, A.; Strukul, G. The Baeyer–Villiger oxidation of ketones: A paradigm for the role of soft Lewis acidity in homogeneous catalysis. *Coord. Chem. Rev.* **2010**, *254*, 646–660. [\[CrossRef\]](#)
6. Kurmach, M.M.; Samotoi, A.O.; Sotnik, S.O.; Terebilenko, A.V.; Yaremov, P.S.; Shvets, O.V.; Shcherban, N.D. Baeyer–Villiger oxidation of cyclic ketones with H₂O₂ over mesoporous Sn- and Zr-BEA zeolites. *Appl. Nanosci.* **2023**, *13*, 6919–6928. [\[CrossRef\]](#)
7. Karcz, R.; Olszowka, J.E.; Napruszewska, B.D.; Kryściak-Czerwenka, J.; Serwicka, E.M.; Klimek, A.; Bahranowski, K. Combined H₂O₂/nitrile/bicarbonate system for catalytic Baeyer–Villiger oxidation of cyclohexanone to ϵ -caprolactone over MgAl hydrotalcite catalysts. *Catal. Commun.* **2019**, *132*, 105821. [\[CrossRef\]](#)
8. Ilovaisky, A.I.; Merkulova, V.M.; Vil', V.A.; Chernoburova, E.I.; Shchetinina, M.A.; Loguzov, S.D.; Dmitrenok, A.S.; Zavarzin, I.V.; Terent'ev, A.O. Regioselective Baeyer–Villiger Oxidation of Steroidal Ketones to Lactones Using BF₃/H₂O₂. *Eur. J. Org. Chem.* **2020**, *2020*, 402–405. [\[CrossRef\]](#)
9. Pembere, A.M.S.; Louis, H.; Wu, H. Mechanism and dynamics of Baeyer–Villiger oxidation of furfural to maleic anhydride in presence of H₂O₂ and Au clusters. *J. Mol. Model.* **2023**, *29*, 359. [\[CrossRef\]](#)
10. Yang, B.; Cui, T. Preparation of extra-large micropore Sn-zeolites and their catalytic performance in Baeyer–Villiger oxidations. *J. Chem. Res.* **2021**, *45*, 269–274. [\[CrossRef\]](#)
11. Burek, B.O.; Bormann, S.; Hollmann, F.; Bloh, J.Z.; Holtmann, D. Hydrogen peroxide driven biocatalysis. *Green Chem.* **2019**, *21*, 3232–3249. [\[CrossRef\]](#)
12. Ten Brink, G.J.; Arends, I.W.C.E.; Sheldon, R.A. The Baeyer–Villiger Reaction: New Developments toward Greener Procedures. *Chem. Rev.* **2004**, *104*, 4105–4124. [\[CrossRef\]](#) [\[PubMed\]](#)
13. Zhang, Q.; Wen, S.; Lei, Z. Heterogeneous Baeyer–Villiger oxidation of ketones using hydrogen peroxide as oxidant catalyzed by aminomethyl polystyrene resin-supported tin complex. *React. Funct. Polym.* **2006**, *66*, 1278–1283. [\[CrossRef\]](#)
14. Wang, J.; Wang, R.; Zhang, Z.; Li, C.; Yang, Z.; Lei, Z. The Influence of Pore Structures and Degree of Crosslinking on Catalytic Properties of Aminomethyl Polystyrene Resins Supported Dendritic Sn Complexes. *J. Macromol. Sci. A* **2008**, *45*, 672–679. [\[CrossRef\]](#)
15. Corma, A.; Navarro, M.T.; Nemeth, L.; Renz, M. Sn-MCM-41—A heterogeneous selective catalyst for the Baeyer–Villiger oxidation with hydrogen peroxide. *Chem. Commun.* **2001**, *21*, 2190–2191. [\[CrossRef\]](#)
16. Li, C.; Wang, J.; Yang, Z.; Hu, Z.; Lei, Z. Baeyer–Villiger oxidation of ketones with hydrogen peroxide catalyzed by cellulose-supported dendritic Sn complexes. *Catal. Commun.* **2007**, *8*, 1202–1208. [\[CrossRef\]](#)
17. Hara, T.; Hatakeyama, M.; Kim, A.; Ichikuni, N.; Shimazu, S. Preparation of clay-supported Sn catalysts and application to Baeyer–Villiger oxidation. *Green Chem.* **2012**, *14*, 771–777. [\[CrossRef\]](#)
18. Yang, X.; Jiang, Y.; Li, Y.; Xu, X.; Li, D.; Lin, K. Mesoporous silica beads containing active and stable tin species for the Baeyer–Villiger oxidations of cyclic ketones. *Micropor. Mesopor. Mat.* **2017**, *253*, 40–48. [\[CrossRef\]](#)
19. Rajalakshmi, R.; Maheswari, R.; Ramanathan, A. Characterization and activity of novel tin incorporated ordered cubic mesoporous silicate, Sn-KIT-6. *Mater. Res. Bull.* **2016**, *75*, 224–229. [\[CrossRef\]](#)
20. Rajalakshmi, R.; Srinivasan, V.V.; Pachamuthu, M.P.; Maheswari, R. Characterizations of tin (SnO₂) doped KIT-5 by direct synthesis. *Mater. Chem. Phys.* **2015**, *154*, 164–169. [\[CrossRef\]](#)
21. Ho, S.-T.; Dinh, Q.-K.; Tran, T.-H.; Nguyen, H.-P.; Nguyen, T.-D. One-step synthesis of ordered Sn-substituted SBA-16 mesoporous materials using prepared silica source of rice husk and their selectively catalytic activity. *Can. J. Chem. Eng.* **2013**, *91*, 34–46. [\[CrossRef\]](#)
22. Pachamuthu, M.P.; Shanthi, K.; Luque, R.; Ramanathan, A. SnTUD-1: A solid acid catalyst for three component coupling reactions at room temperature. *Green Chem.* **2013**, *15*, 2158–2166. [\[CrossRef\]](#)
23. Chen, T.; Wang, B.; Li, Y.; Liu, L.; Qiu, S. Hydrothermal synthesis of tin containing mesoporous silicas and their catalytic performance over Baeyer–Villiger oxidation of cyclohexanone to ϵ -caprolactone: Comparison of Sn/MCM-41 and Sn/SBA-15. *J. Porous. Mat.* **2015**, *22*, 949–957. [\[CrossRef\]](#)
24. Jiang, N.; Koo, J.-B.; Han, S.-C.; Park, S.-E. Lewis-type catalytic activity of direct incorporated Zr- and Sn-SBA-16 catalysts. *Res. Chem. Intermediat.* **2008**, *34*, 507–517. [\[CrossRef\]](#)
25. Nandiyanto, A.B.D.; Okuyama, K. Progress in developing spray-drying methods for the production of controlled morphology particles: From the nanometer to submicrometer size ranges. *Adv. Powder Technol.* **2011**, *22*, 1–19. [\[CrossRef\]](#)
26. Lwin, S.; Wachs, I.E. Olefin Metathesis by Supported Metal Oxide Catalysts. *ACS Catal.* **2014**, *4*, 2505–2520. [\[CrossRef\]](#)
27. Pega, S.; Boissière, C.; Grosso, D.; Azaïs, T.; Chaumonnot, A.; Sanchez, C. Direct Aerosol Synthesis of Large-Pore Amorphous Mesoporous Aluminosilicates with Superior Acid-Catalytic Properties. *Angew. Chem. Int. Ed.* **2009**, *121*, 2822–2825. [\[CrossRef\]](#)

28. Debecker, D.P.; Stoyanova, M.; Colbeau-Justin, F.; Rodemerck, U.; Boissière, C.; Gaigneaux, E.M.; Sanchez, C. One-Pot Aerosol Route to $\text{MoO}_3\text{-SiO}_2\text{-Al}_2\text{O}_3$ Catalysts with Ordered Super Microporosity and High Olefin Metathesis Activity. *Angew. Chem. Int. Ed.* **2012**, *51*, 2129–2131. [\[CrossRef\]](#)
29. Godard, N.; Vivian, A.; Fusaro, L.; Cannavici, L.; Aprile, C.; Debecker, D.P. High-Yield Synthesis of Ethyl Lactate with Mesoporous Tin Silicate Catalysts Prepared by an Aerosol-Assisted Sol–Gel Process. *ChemCatChem* **2017**, *9*, 2211–2218. [\[CrossRef\]](#)
30. Garcia Marquez, A.; Horcajada, P.; Grosso, D.; Ferey, G.; Serre, C.; Sanchez, C.; Boissiere, C. Green scalable aerosol synthesis of porous metal–organic frameworks. *Chem. Commun.* **2013**, *49*, 3848–3850. [\[CrossRef\]](#)
31. Meng, Q.; Liu, J.; Liu, L.; Xiong, G. Aerosol-assisted hydrothermal synthesis of hierarchical Sn-Beta nanoaggregates in fluoride media. *Micropor. Mesopor. Mat.* **2021**, *320*, 111090. [\[CrossRef\]](#)
32. Iskandar, F.; Gradon, L.; Okuyama, K. Control of the morphology of nanostructured particles prepared by the spray drying of a nanoparticle sol. *J. Colloid Interf. Sci.* **2003**, *265*, 296–303. [\[CrossRef\]](#) [\[PubMed\]](#)
33. Fang, J.; Dong, H.; Xu, H. The effect of Lewis acidity of tin loading siliceous MCM-41 on glucose conversion into 5-hydroxymethylfurfural. *Renew. Energy* **2023**, *218*, 119305. [\[CrossRef\]](#)
34. Candela-Noguera, V.; Alfonso, M.; Amorós, P.; Aznar, E.; Marcos, M.D.; Martínez-Mañez, R. In-depth study of factors affecting the formation of MCM-41-type mesoporous silica nanoparticles. *Micropor. Mesopor. Mat.* **2024**, *363*, 112840. [\[CrossRef\]](#)
35. Cheng, W.; Jiang, Y.; Xu, X.; Wang, Y.; Lin, K.; Pescarmona, P.P. Easily recoverable titanosilicate zeolite beads with hierarchical porosity: Preparation and application as oxidation catalysts. *J. Catal.* **2016**, *333*, 139–148. [\[CrossRef\]](#)
36. Trong On, D.; Nguyen, S.V.; Hulea, V.; Dumitriu, E.; Kaliaguine, S. Mono- and bifunctional MFI, BEA and MCM-41 titanium-molecular sieves. Part 1. Synthesis and characterization. *Micropor. Mesopor. Mat.* **2003**, *57*, 169–180. [\[CrossRef\]](#)
37. Boronat, M.; Concepción, P.; Corma, A.; Navarro, M.T.; Renz, M.; Valencia, S. Reactivity in the confined spaces of zeolites: The interplay between spectroscopy and theory to develop structure–activity relationships for catalysis. *Phys. Chem. Chem. Phys.* **2009**, *11*, 2876–2884. [\[CrossRef\]](#)
38. Kang, Z.; Zhang, X.; Liu, H.; Qiu, J.; Han, W.; Yeung, K.L. Factors affecting the formation of Sn-Beta zeolites by steam-assisted conversion method. *Mater. Chem. Phys.* **2013**, *141*, 519–529. [\[CrossRef\]](#)
39. Zhou, S.; Zhou, L.; Su, Y.; Yang, X.; He, H. Effect of silica source on the synthesis, property and catalytic performance of Sn-Beta zeolite. *Mater. Chem. Phys.* **2021**, *272*, 124995. [\[CrossRef\]](#)
40. Zhu, Z.; Xu, H.; Jiang, J.; Guan, Y.; Wu, P. Sn-Beta zeolite hydrothermally synthesized via interzeolite transformation as efficient Lewis acid catalyst. *J. Catal.* **2017**, *352*, 1–12. [\[CrossRef\]](#)
41. Smeets, V.; Boissière, C.; Sanchez, C.; Gaigneaux, E.M.; Peeters, E.; Sels, B.F.; Dusselier, M.; Debecker, D.P. Aerosol Route to $\text{TiO}_2\text{-SiO}_2$ Catalysts with Tailored Pore Architecture and High Epoxidation Activity. *Chem. Mater.* **2019**, *31*, 1610–1619. [\[CrossRef\]](#)
42. Xu, H.; Wang, X.; Ji, P.; Wu, H.; Guan, Y.; Wu, P. Hydrothermal synthesis of Sn-Beta zeolites in F^- -free medium. *Inorg. Chem. Front.* **2018**, *5*, 2763–2771. [\[CrossRef\]](#)
43. Yuan, E.-H.; Li, M.; Zhou, J.-F.; Niu, Y.; Song, Y.-H.; Zhang, K.; Yang, M.-H.; Jiang, J.; Zhang, B.; Xiao, F.-S.; et al. Ultrafast crystallization of mesoporous Sn-MFI single crystals achieved by addition of the cationic polyelectrolyte in starting gels. *Micropor. Mesopor. Mat.* **2022**, *337*, 111922. [\[CrossRef\]](#)
44. Xiong, G.; Yang, H.; Liu, L.; Liu, J. Post-synthesis of Sn-beta zeolite by aerosol method. *RSC Adv.* **2023**, *13*, 4835–4842. [\[CrossRef\]](#) [\[PubMed\]](#)
45. Concepción, P.; Pérez, Y.; Hernández-Garrido, J.C.; Fajardo, M.; Calvino, J.J.; Corma, A. The promotional effect of Sn-beta zeolites on platinum for the selective hydrogenation of α,β -unsaturated aldehydes. *Phys. Chem. Chem. Phys.* **2013**, *15*, 12048–12055. [\[CrossRef\]](#)
46. Vivian, A.; Soumoy, L.; Fusaro, L.; Fiorilli, S.; Debecker, D.P.; Aprile, C. Surface-functionalized mesoporous gallosilicate catalysts for the efficient and sustainable upgrading of glycerol to solketal. *Green Chem.* **2021**, *23*, 354–366. [\[CrossRef\]](#)

Disclaimer/Publisher’s Note: The statements, opinions and data contained in all publications are solely those of the individual author(s) and contributor(s) and not of MDPI and/or the editor(s). MDPI and/or the editor(s) disclaim responsibility for any injury to people or property resulting from any ideas, methods, instructions or products referred to in the content.